Electrochemical reduction of CO2 catalyzed by Fe-N-C materials: a structure-selectivity study

Tran Ngoc Huan, Nastaran Ranjbar, Gwenaelle Rousse, Moulay Tahar Sougrati, Andrea Zitolo, Victor Mougel, Frederic Jaouen, Marc Fontecave

Electrochemical Reduction of CO_2 Catalyzed by Fe-N-C Materials: a Structure-Selectivity Study

Tran Ngoc Huan,[1] Nastaran Ranjbar,[2] Gwenaëlle Rousse,[3] Moulay Sougrati,[2] Andrea Zitolo,[4] Victor Mougel,[1] Frédéric Jaouen,[2] Marc Fontecave[1]**

[1]Laboratoire de Chimie des Processus Biologiques, UMR CNRS 8229, Collège de France, Université Pierre et Marie Curie, 11 Place Marcelin Berthelot, 75005 Paris, France.

[2]Institut Charles Gerhardt Montpellier, UMR CNRS 5253, Université Montpellier, 2 place Eugène Bataillon 34095 Montpellier, France

[3] Laboratoire Chimie du Solide et Energie, CNRS FRE 3677, Collège de France, Université Pierre et Marie Curie, 11 Place Marcelin Berthelot, 75005 Paris, France.

[4] Synchrotron SOLEIL, L'Orme des Merisiers Saint-Aubin - BP 48, 91192 Gif-sur-Yvette, France

ABSTRACT: Selective electrochemical reduction of CO_2 into energy-dense organic compounds is a promising strategy for using CO_2 as a carbon source. Herein, we investigate a series of iron-based catalysts synthesized by pyrolysis of Fe-, N- and C- containing precursors for the electroreduction of CO_2 to CO in aqueous conditions and demonstrate that the selectivity of these materials for CO_2 reduction over proton reduction is governed by the ratio of isolated FeN_4 sites vs. Fe-based nanoparticles. This ratio can be synthetically tuned to generate electrocatalysts producing controlled CO/H_2 ratios. It notably allows preparing materials containing only FeN_4 sites, which are able to selectively reduce CO_2 to CO in aqueous solution with Faradaic yields over 90% and at low overpotential.

KEYWORDS. CO_2 reduction – electrocatalysis – iron - Fe-N-C materials – Structure-selectivity relationship.

INTRODUCTION

Electroreduction of CO_2 into energy-dense liquid or gaseous fuels as a way to store energy from intermittent sources has received renewed attention in the past few years. However, its practical implementation into technological devices (photoelectrochemical cells or electrolyzers coupled to photovoltaics) is highly challenging due to the inertness of CO_2 and the multiple electron and proton transfers required for its transformation. Efficient catalysts and appropriate reaction conditions (solvent, temperature…) must be developed to efficiently mediate these transfers, while keeping selectivity over the competing proton reduction into dihydrogen.[1-4] In that context, conversion of CO_2 into CO is an attractive target as it requires the transfer of only two electrons and two protons. CO finds many applications in bulk chemicals manufacturing and for the preparation of synthetic fuels via Fischer-Tropsch processes.

Recently, catalysts based on earth abundant metals that are integrated in, or supported on, carbon materials have been identified as promising alternatives to noble metal catalysts (Au, Ag) for reducing CO_2 in aqueous conditions.[5-16] In that context, Fe-N-C materials obtained by pyrolysis of Fe-, N- and C- containing precursors have been predicted[14] and reported[15] to be highly efficient for this transformation. However, one aspect limiting the rational development of Metal-N-C materials prepared *via* pyrolytic synthetic strategies is the identification of the actual active species. Numerous studies have indeed shown that these materials are often inhomogeneous and typically contain a significant amount of segregated and crystallographically–ordered structures of the metal (reduced metal, carbides, nitrides, etc…) along with atomically-dispersed metal ions hosted in the carbon matrix and coordinated with N and/or C atoms.[17] The simultaneous presence of several metal-based components in such materials has for a long time prevented the clear identification of the key actors in their overall activity and selectivity toward oxygen reduction.[18-20] The same challenge now applies to the identification of the sites in Metal-N-C materials that are active toward CO_2 reduction[15] and/or active toward the competing hydrogen evolution reaction.

In this work, we focused on the understanding of the structural parameters ruling the selectivity toward CO_2 electroreduction of pyrolyzed Fe-N-C materials. For that purpose we synthesized and characterized structurally and electrochemically a set of Fe-N-C materials with a variable proportion of single-Fe-atom centers and Fe-containing nanoparticles (Figure 1). This variety of Fe species was obtained by varying either the Fe content or the homogenization procedure of precursors carried out before the pyrolysis step. This series of materials allowed us establishing a structure-selectivity relationship for CO_2 reduction. We have here identified FeN_4 moieties as the key active sites for the selective CO_2 reduction into CO in aqueous conditions, while Fe nanoparticles mainly catalyze hydrogen evolution. The material containing FeN_4 moieties as the sole Fe species reached a Faradaic yield (FY) for CO formation of 91 %, one of the highest reported hitherto for either precious[21-24] or non-precious metal catalysts.[6,7,9,15] In addition, we have demonstrated that the CO/H_2 product ratio, an important parameter for the potential use as syngas for Fischer- Tropsch processes, can be easily controlled by tuning the ratio of FeN_4 moieties *vs* iron nanoparticles in Fe-N-C materials.

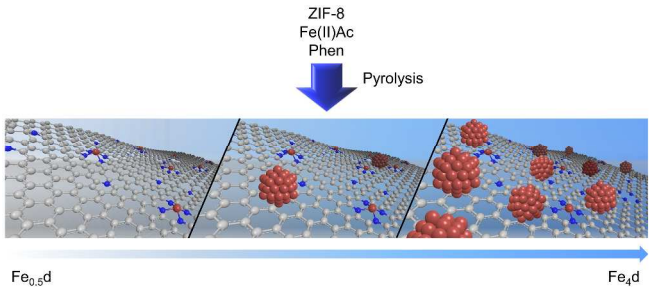

Figure 1. Schematic representation of the various Fe-N-C materials obtained upon pyrolysis: the amount of Fe nanoparticles increases with increased Fe loading. Fe atoms are represented in red, C atoms in grey and N atoms in blue. The graphitic shell typically surrounding Fe nanoparticles after pyrolysis is not represented for clarity.

RESULTS and DISCUSSION

Preparation of Fe-N-C materials

All Fe-N-C materials of this study were prepared from a Zn-based zeolitic imidazolate framework (ZIF-8), ferrous acetate and phenanthroline, as described in detail in the Supporting information section. We synthesized and studied five different Fe-based materials, labeled $Fe_{4.0}d$, $Fe_{1.0}w$, $Fe_{1.0}d$, $Fe_{0.5}d$ and $Fe_{0.5}d$-950 according to the synthetic conditions. The subscript 0.5, 1.0 or 4.0 corresponds to the weight % Fe in the catalyst precursor, before pyrolysis. The final letter w (wet) or d (dry) indicates whether a wet impregnation step was applied (w) or not (d) before the milling step used for mixing ZIF-8, ferrous acetate and phenanthroline. The first four materials were prepared by pyrolysis in flowing Ar at 1050°C. An iron-free nitrogen-doped carbon material, labeled $Fe_{0.0}d$, was prepared similarly by using only ZIF-8 and phenanthroline as precursors. The fifth Fe-containing material, namely $Fe_{0.5}d$-950, was prepared by subjecting $Fe_{0.5}d$ to a second pyrolysis step in flowing ammonia at 950°C.

Powder X-ray diffraction (XRD) spectra (Figure S1) revealed the presence of a crystalline Fe-based structure (Fe_3C) only in the sample with the highest Fe content, namely $Fe_{4.0}d$, while for all other catalysts the diffractograms showed only two broad reflection peaks typical for the nanometric graphitic domains of amorphous N-doped carbon materials. As shown later in this work, the absence of diffraction peaks assigned to Fe structures does however not rule out the presence of non-crystalline FeN_xC_y moieties or even of low amounts of crystalline Fe, due to the low sensitivity of powder XRD. We then resorted to ^{57}Fe Mössbauer spectroscopy and extended X-ray absorption fine structure (EXAFS), that are more sensitive and appropriate to identify the coordination of isolated Fe ions not embedded in a crystalline iron structure.

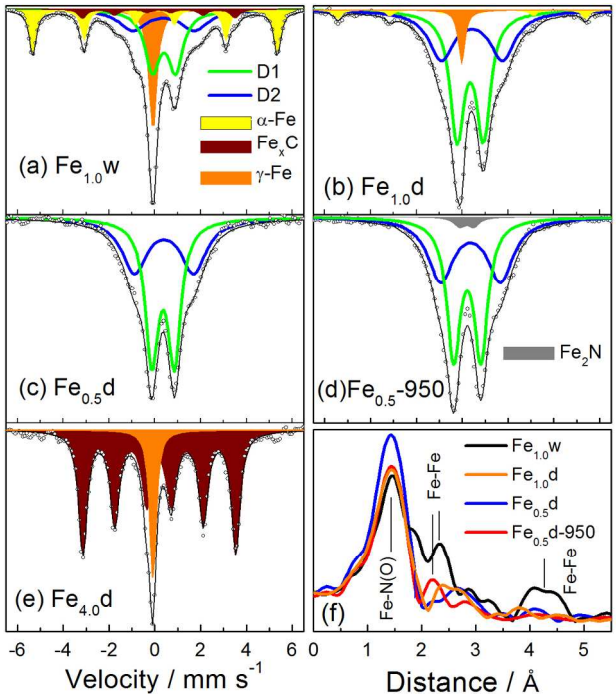

Figure 2. a-e) ^{57}Fe Mössbauer absorption spectra of the Fe-N-C materials, as labeled on the figure. f) k^2-weighted Fourier transforms of the experimental EXAFS spectra. Mössbauer and EXAFS spectra of $Fe_{1.0}d$, $Fe_{0.5}d$, $Fe_{0.5}d$-950 and $Fe_{1.0}w$ have been already reported separately,[17,25] but are presented again here together for easier comparisons between all samples.

The Mössbauer spectra of the five Fe-N-C samples are shown in Figure 2a-e. In contrast with XRD, Mössbauer spectroscopy reveals the presence of Fe crystalline structures for all catalysts but $Fe_{0.5}d$. It also shows the presence of atomically dispersed Fe ions in the N-doped carbon matrix, namely square-planar $Fe(II)N_4$ or $Fe(III)N_4$ species in a low- and medium-spin state, respectively (doublets D1, D2; see Table S1 for isomer shift and quadrupole splitting values) in all catalysts except $Fe_{4.0}d$. In the case of $Fe_{1.0}w$, the spectra could be fitted with two sextets assigned to α-Fe and iron carbide Fe_xC, one singlet assigned to γ-Fe and the two doublets D1 and D2. The Mössbauer parameters for the sextets and the singlet are indeed characteristic for such Fe structures.[17] The doublets are much more intense in the spectrum of $Fe_{1.0}d$ (Figure 2b as compared to 2a), highlighting the differences between the wet and dry homogenization methods. Formation of Fe crystalline structures is further decreased by decreasing the Fe content: the spectrum of $Fe_{0.5}d$ is fitted with only D1 and D2. Subjecting $Fe_{0.5}d$ to an additional pyrolysis step in NH_3 ($Fe_{0.5}$-950) did not change noticeably the Fe speciation, but an additional doublet D3 accounting for only 3% of the total intensity is observed and could be assigned to crystalline Fe_2N or $Fe_{2+x}N$ nanoparticles (Table S1). Last, the Mössbauer spectrum of $Fe_{4.0}d$ clearly shows that this sample contains mainly iron carbide, as previously indicated by powder XRD, and no discernible amount of isolated FeN_4 species. Table 1 summarizes the Fe content and speciation of the different samples, as obtained from X-ray absorption and Mössbauer spectroscopy, respectively.

Table 1. Fe content and Fe speciation within the different materials determined by ^{57}Fe Mössbauer spectroscopy (Samples listed by increasing absolute content of FeN_4 moieties).

Material	Total Fe content / wt%[a]	FeN_4 content / wt % (relative %)[b]	Crystalline Fe content/ wt % (relative %)[b]
$Fe_{0.5}d$	1.5	1.5 (100 %)	0.0 (0 %)
$Fe_{0.5}d$-950	2.1	2.0 (97 %)	0.1 (3 %)
$Fe_{1.0}d$	3.4	3.1 (92 %)	0.3 (8 %)
$Fe_{1.0}w$	3.0	1.6 (53 %)	1.4 (47 %)
$Fe_{4.0}d$	12.0	0.00 (0 %)	12.0 (100 %)

[a] The total Fe content of each sample was derived from the height of the absorption peak when performing X-ray absorption in transmission mode. [b] The relative contents of FeN_4 moieties (D1 and D2) and Fe nanoparticles (Fe_3C, α-Fe, γ-Fe and Fe_2N) were then derived from the absorption area of respective components in the Mössbauer spectra. The absolute content of FeN_4 moieties and Fe nanoparticles were then obtained by multiplying their relative % by the total Fe content of each sample.

In order to further identify the materials containing isolated FeN_4 moieties, these were characterized by X-ray absorption spectroscopy at the Fe K-edge, and the k^2-weighted Fourier transforms of their EXAFS function are shown in Figure 2f. While a very detailed XANES and EXAFS analysis of these materials is extremely complex due to the presence of mixtures of Fe species in most of them, qualitative analysis of the XAS spectra provides important insights on the nature of the surface species. The four samples $Fe_{1.0}w$, $Fe_{1.0}d$, $Fe_{0.5}d$ and $Fe_{0.5}d$-950 show a first intense signal at *ca* 1.4 Å (non-corrected for phase shift), assigned to Fe-N backscattering, typical for $Fe(II)N_4$ sites[17] in line with Mössbauer spectroscopy data (Figure 2a-d). The presence of a signal at a longer bond distance of 2.2-2.4 Å (non-corrected for phase shift) also confirms the presence of iron-based crystalline structures in $Fe_{1.0}w$, $Fe_{1.0}d$ and $Fe_{0.5}d$-950, which was observed by Mössbauer spectroscopy (Figures 2a-2b-2d). For $Fe_{1.0}w$ and $Fe_{1.0}d$, the signal at 2.3-2.4 Å can be assigned to Fe-Fe backscattering from α-Fe (8 Fe atoms in the first coordination sphere at 2.48 Å and 6 Fe atoms in the second coordination sphere at 2.87 Å) and γ-Fe (12 Fe atoms in the first coordination sphere at 2.52 Å). For $Fe_{0.5}d$-950, the weak signal at 2.2 Å can be assigned to Fe-Fe backscattering signal from crystalline iron nitrides, as previously observed for analogous materials.[17] Fitting of the EXAFS function allowed determining an Fe-Fe bond distance of 2.7 Å in this iron nitride crystalline phase (present in minor amount), in agreement with the separately determined bond distance in Fe_2N.[26] In contrast, the Fourier transform of the EXAFS function for $Fe_{0.5}d$ revealed the absence of Fe-Fe backscattering signals, the signal at *ca* 2.7 Å being assigned to Fe-C backscattering (second coordination sphere of Fe in FeN_xC_y moieties) rather than to a possible Fe-Fe interaction (*e.g.* due to the second coordination sphere in crystalline Fe structures).[17] The EXAFS characterization of $Fe_{0.5}d$ therefore supports the previous conclusion that the two doublets seen in its Mössbauer spectrum can be associated with two different types of FeN_xC_y moieties, representing a ferrous or ferric ion strongly coordinated with a light element (most probably nitrogen atoms) and covalently integrated in the carbon matrix.

Transmission electron microscopy (TEM) images confirmed Mössbauer and EXAFS analyses, as crystalline Fe nanoparticles are clearly observed in the materials containing higher Fe contents (Figure S2a) but not in $Fe_{0.5}d$ (Figure S2b).[25 27]

For electrochemical characterization, a thin film of these materials was deposited on a carbon-based gas diffusion layer (GDL), using a Nafion® binder (see supporting information). The binder did not modify significantly the morphology of the GDL, as shown by scanning electron microscopy (SEM) (Figure S2c).

CO_2 electrocatalytic reduction

The electrocatalytic activity of the materials supported on GDL for CO_2 reduction was probed by linear sweep voltammetry (LSV) in CO_2–saturated 0.5 M $NaHCO_3$ solutions. Catalytic waves were observed for all Fe-containing materials but not for the control $Fe_{0.0}d$ material (Figure 3). Onset potentials allow us identifying two groups of materials, with $Fe_{1.0}d$, $Fe_{0.5}d$ and $Fe_{0.5}d$-950 characterized by low onset potentials of -0.3 V vs. RHE (190 mV overpotential for CO_2/CO), and $Fe_{1.0}w$ and $Fe_{4.0}d$ characterized by high onset potentials of -0.5 V vs. RHE. Furthermore, below the onset potential, current densities increased more rapidly with decreasing potential in the case of the second group. This supports the idea that these two set of materials catalyze different reactions, as will be evidenced later.

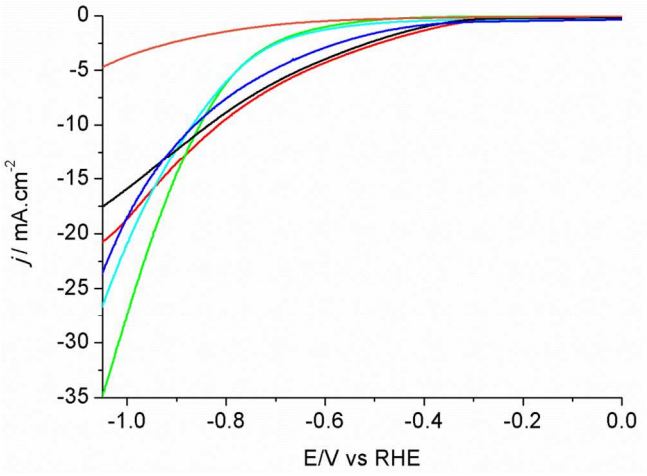

Figure 3: LSV of metal-free $Fe_{0.0}d$ (orange), $Fe_{4.0}d$ (green), $Fe_{1.0}w$ (cyan), $Fe_{1.0}d$ (red), $Fe_{0.5}d$-950 (black) and $Fe_{0.5}d$ (blue) in CO_2-saturated 0.5 M $NaHCO_3$ aqueous solutions.

Further characterization of the catalysed reactions was provided by controlled-potential electrolysis (CPE) (Figure S3). Figures 4a and 4b report the Faradaic Yields (FY) of the materials for CO and H_2 production after 5 minutes electrolysis[28] in a 0.5 M $NaHCO_3$ aqueous solution for potentials between -0.4 V and -1.0 V *vs.* RHE. These data point to very different behaviours between the various catalysts: while, for any catalyst, CO2 reduction to CO optimally occurs at *ca*. -0.5 to -0.6 V vs. RHE and is less selective upon scanning towards more cathodic potential, the absolute FY for CO formation in that potential region strongly depends on the catalyst. The highest selectivity for CO production (FY up to 80 % at -0.5 V *vs.* RHE) is obtained with $Fe_{0.5}d$ and $Fe_{0.5}d$-950. We note that these two catalysts are those that contain the highest relative fraction of Fe in the form of FeN_4 moieties (97-100 %, Table 1). In contrast, the catalysts that contain a large relative fraction of Fe in the form of crystalline Fe ($Fe_{1.0}w$ and $Fe_{4.0}d$, 47 and 100 %, Table 1) result in a high FY for H_2 at all potentials (Figure 4b). Control experiments using GDL supporting $Fe_{0.0}d$ produced CO as the major product (FY= 80% at -1.0V vs. RHE), however with very low production rates (low current densities) (Figure S4).

In addition, for all catalysts, CO production rate reaches a maximum at -0.8 V vs. RHE (Figure S5), indicative of similar active sites for CO production in all catalysts.

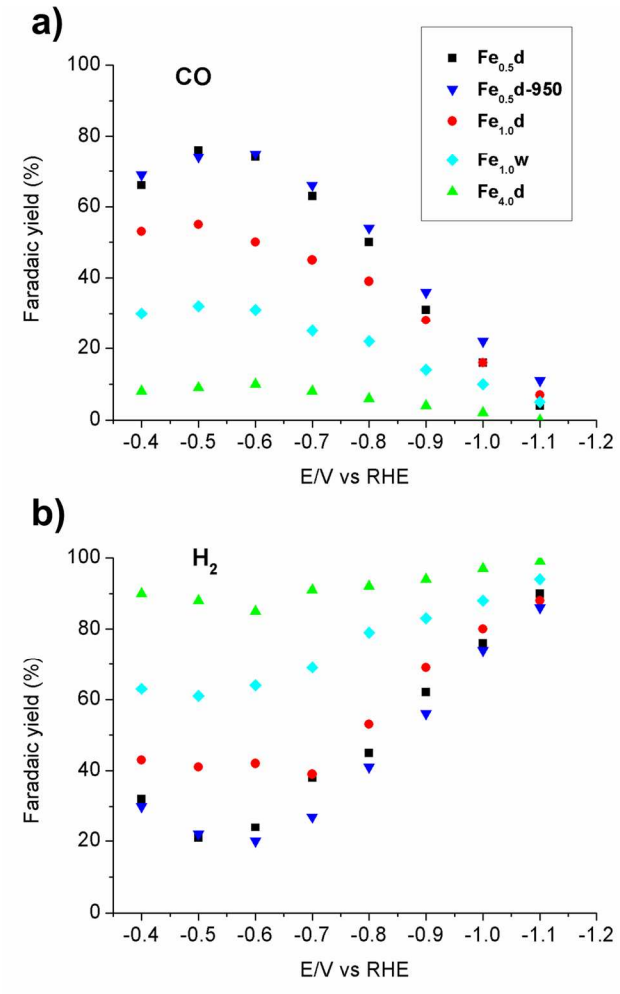

Figure 4. Faradaic yield for CO (a) and H_2 (b) formation after 5 minutes CPE during CO_2 reduction in CO_2–saturated 0.5 M $NaHCO_3$ using $Fe_{0.5}$d (black), $Fe_{0.5}$d-950 (blue), $Fe_{1.0}$d (red), $Fe_{1.0}$w (cyan) and $Fe_{4.0}$d (green).

It should be noted that when electrolysis using $Fe_{0.5}$d electrode was carried out in the absence of CO_2 (N_2-saturated 0.5 M $NaHCO_3$ solution), H_2 was the sole product (FY 100%) from -0.3 to -1.0 V vs RHE. This demonstrates that CO formation is intimately linked to CO_2 reduction, and excludes the possible formation of CO as a result of the decomposition or transformation of the carbon structure from GDL or from the catalyst themselves. As shown in Figure S6, CH_4 was also observed as a minor product during electrolyses. The highest FY for CH_4 (up to 1.5%) was obtained with the $Fe_{0.5}$ electrodes at -1.0V vs. RHE.

The ratio of FeN_4 moieties to Fe-based nanoparticles in these materials therefore seems to control the selectivity for CO formation relative to hydrogen evolution. This is clearly demonstrated in Figure 5, showing an increased CO/H_2 ratio with increased relative content of FeN_4 moieties. The sharp drop in CO/H_2 ratio when the relative content of FeN_4 is < 97 % can be assigned to the lower Tafel slope for H_2 evolution than for CO_2 reduction to CO. A small relative content of Fe nanoparticles can thus lead to a high yield of H_2 formation. While it is unclear whether all or only some Fe-based crystalline structures catalyze the H_2 evolution, the identification of the latter as H_2 evolution sites is in line with recent reports on the H_2 evolution activity in acid medium of Fe particles protected by a thin graphitic shell.[29,30]

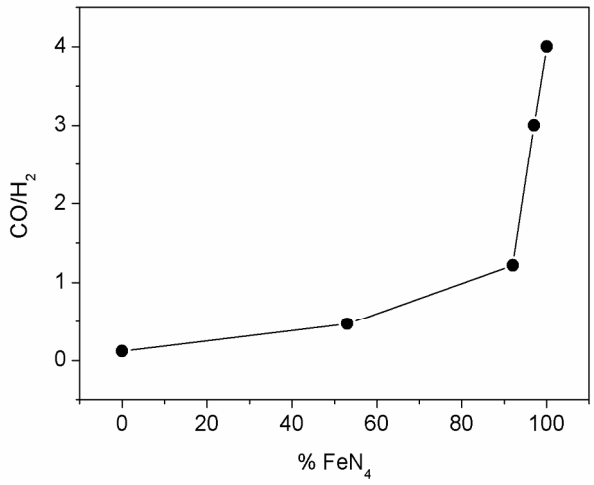

Figure 5. CO/H_2 ratio of the gas blend formed after 5 minutes of electrolysis at -0.5 V vs RHE of aqueous solution of CO_2 (0.1 M $NaHCO_3$) as a function of the relative content of FeN_4 sites over the total iron content in the materials.

In addition, the selectivity of the reaction towards CO formation could be further improved using less concentrated electrolyte (Figure 6), in agreement with a recent report.[31] This led to a FY for CO of 91 % at -0.6 V vs. RHE using $Fe_{0.5}$d in 0.1 M $NaHCO_3$, however at the expense of a lower current density and CO production rate (7.5 $mA.cm^{-2}$ and 2.9 $nmol_{CO}.s^{-1}$ in 0.5 M $NaHCO_3$ vs. 4.5 $mA.cm^{-2}$ and 2.1 $nmol_{CO}.s^{-1}$ in 0.1 M $NaHCO_3$, Figure S7).

A recently reported Fe-N-C catalyst prepared by a different route, *via* multi-pyrolysis and multi acid leaching of an Fe salt, polyaniline and Ketjenblack[15] displayed a selectivity for CO_2 reduction to CO of *ca* 80 % at -0.6 V *vs* RHE in 0.1 M KHCO3 (Fig. 4e in Ref 15). That material contains 83 % FeN_4 sites,[32,33] and its selectivity for CO is hence in good agreement with those reported here and with the identification by Varela *et al* of Metal-N4 moieties as the active site for selective CO_2 to CO reduction. A larger difference in selectivity was however observed at -0.8 V *vs* RHE: 60 % FY was measured for $Fe_{0.5}$d in the present study while *ca.* 38 % FY was observed for the Fe-N-C sample in Ref. 15, both measured in 0.1 M bicarbonate electrolyte. In view of the present study, we propose that these differences can be due to the presence of a minor fraction of Fe crystalline structures in the latter, as confirmed by the Mössbauer spectrum.[32, 33]

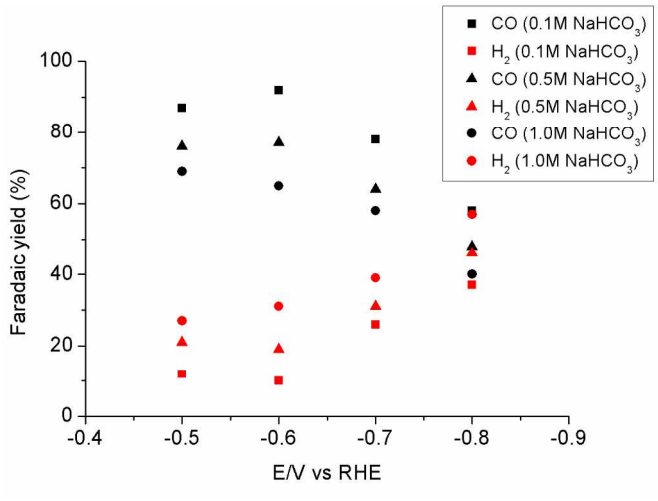

Figure 6. Faradaic yield for CO (black) and H_2 (red) at different potentials using $Fe_{0.5}$d in aqueous $NaHCO_3$ electrolytes with molarities of 0.1 M (square), 0.5 M (triangle), 1.0 M (circle).

Finally, in order to assess the stability of the best material for CO_2 reduction, a longer electrolysis experiment was carried out at -0.6 V vs. RHE using $Fe_{0.5}$d (0.5 M $NaHCO_3$, continuous CO_2 bubbling). As shown in Figure S8, the current density remained stable at *ca* 6 $mA.cm^{-2}$ during 6 h, and CO production rate maintained steady at 25 $nmol.s^{-1}$.

CONCLUSION

Fe-N-C materials recently appeared as promising materials for CO_2 reduction and the parameters chosen for their synthesis appear critical, since such materials are generally heterogeneous in terms of Fe speciation. In an effort to direct their synthesis towards the most selective materials, we have investigated here the effect of the Fe speciation on the catalytic selectivity by a combined structural and catalytic characterization of a broad variety of Fe-N-C materials. We clearly identified isolated FeN_4 sites as the critical catalytic species for the selective electrochemical reduction of CO_2 to CO. From that study, the $Fe_{0.5}$d material proved the most effective and selective catalyst, producing CO with high FY (up to 90%), low overpotentials (190 mV overpotential relative to the formal equilibrium potential for CO_2/CO in 0.5 M $NaHCO_3$ aqueous solution) and sustaining long-term electrolysis. Interestingly these sites are reminiscent of soluble Fe-porphyrins which proved excellent catalysts for catalytic CO_2 conversion to CO.[6,34] In contrast, materials carrying metallic Fe particles (or iron carbides) are mainly active for proton reduction under similar conditions. This can be easily exploited to generate materials producing a gas mixture with a targeted H_2/CO ratio. Controlling this ratio could be critical for use of the H_2/CO gas mixture in Fischer Tropsch processes, different ratio being required depending on the catalyst used for the downstream chemical transformation of CO into various products.[35]

General information, procedures and characterization data.

AUTHOR INFORMATION

Corresponding Author

* frederic.jaouen@univ-montp2.fr, marc.fontecave@college-de-france.fr

ASSOCIATED CONTENT

The supporting Information is available free of charge via the Internet at http://pubs.acs.org.

ACKNOWLEDGMENT

We acknowledge Synchrotron SOLEIL (Gif-sur Yvette, France) for provision of synchrotron radiation facilities at beamline SAMBA (proposal 20131078). We thank Dr Philippe Simon for support with GC analyses.

REFERENCES

(1) Qiao, J. L.; Liu, Y. Y.; Hong, F.; Zhang, J. J. *Chem. Soc. Rev.* **2014**, *43*, 631-675.
(2) Benson, E. E.; Kubiak, C. P.; Sathrum, A. J.; Smieja, J. M. *Chem. Soc. Rev.* **2009**, *38*, 89-99.
(3) Kuhl, K. P.; Hatsukade, T.; Cave, E. R.; Abram, D. N.; Kibsgaard, J.; Jaramillo, T. F. *J. Am. Chem. Soc.* **2014**, *136*, 14107-14113.
(4) Huan, T. N.; Simon, P.; Rousse, G.; Génois, I.; Artero, V.; Fontecave, M. *Chem. Sci.* **2017**, *8*, 742-747.
(5) Cheng, M.-J.; Kwon, Y.; Head-Gordon, M.; Bell, A. T. *J. Phys. Chem. C* **2015**, *119*, 21345-21352.
(6) Costentin, C.; Drouet, S.; Robert, M.; Savéant, J.-M. *Science* **2012**, *338*, 90-94.
(7) Lin, S.; Diercks, C. S.; Zhang, Y.-B.; Kornienko, N.; Nichols, E. M.; Zhao, Y.; Paris, A. R.; Kim, D.; Yang, P.; Yaghi, O. M.; Chang, C. J. *Science* **2015**, *349*, 1208-1213.
(8) Morlanés, N.; Takanabe, K.; Rodionov, V. *ACS Catal.* **2016**, *6*, 3092-3095.
(9) Oh, S.; Gallagher, J. R.; Miller, J. T.; Surendranath, Y. *J. Am. Chem. Soc.* **2016**, *138*, 1820-1823.
(10) Shen, J.; Kortlever, R.; Kas, R.; Birdja, Y. Y.; Diaz-Morales, O.; Kwon, Y.; Ledezma-Yanez, I.; Schouten, K. J. P.; Mul, G.; Koper, M. T. M. *Nat. Commun.* **2015**, *6*, 8177.
(11) Song, Y.; Peng, R.; Hensley, D. K.; Bonnesen, P. V.; Liang, L.; Wu, Z.; Meyer, H. M.; Chi, M.; Ma, C.; Sumpter, B. G.; Rondinone, A. J. *ChemistrySelect* **2016**, *1*, 6055-6061.
(12) Sun, X. F.; Kang, X. C.; Zhu, Q. G.; Ma, J.; Yang, G. Y.; Liu, Z. M.; Han, B. X. *Chem. Sci.* **2016**, *7*, 2883-2887.
(13) Tatin, A.; Comminges, C.; Kokoh, B.; Costentin, C.; Robert, M.; Savéant, J.-M. *Proceedings of the National Academy of Sciences* **2016**, *113*, 5526-5529.
(14) Tripkovic, V.; Vanin, M.; Karamad, M.; Björketun, M. E.; Jacobsen, K. W.; Thygesen, K. S.; Rossmeisl, J. *J. Phys. Chem. C* **2013**, *117*, 9187-9195.
(15) Varela, A. S.; Ranjbar Sahraie, N.; Steinberg, J.; Ju, W.; Oh, H.-S.; Strasser, P. *Angew. Chem. Int. Ed.* **2015**, *54*, 10758-10762.
(16) Weng, Z.; Jiang, J.; Wu, Y.; Wu, Z.; Guo, X.; Materna, K. L.; Liu, W.; Batista, V. S.; Brudvig, G. W.; Wang, H. *J. Am. Chem. Soc.* **2016**, *138*, 8076-8079.
(17) Zitolo, A.; Goellner, V.; Armel, V.; Sougrati, M.-T.; Mineva, T.; Stievano, L.; Fonda, E.; Jaouen, F. *Nat Mater* **2015**, *14*, 937-942.
(18) Lefèvre, M.; Proietti, E.; Jaouen, F.; Dodelet, J.-P. *Science* **2009**, *324*, 71-74.
(19) Lin, L.; Yang, Z. K.; Jiang, Y.-F.; Xu, A.-W. *ACS Catal.* **2016**, *6*, 4449-4454.
(20) Jaouen, F.; Proietti, E.; Lefevre, M.; Chenitz, R.; Dodelet, J. P.; Wu, G.; Chung, H. T.; Johnston, C. M.; Zelenay, P. *Energy Environ. Sci.* **2011**, *4*, 114-130.
(21) Hall, A. S.; Yoon, Y.; Wuttig, A.; Surendranath, Y. *J. Am. Chem. Soc.* **2015**, *137*, 14834-14837.
(22) Rosen, B. A.; Salehi-Khojin, A.; Thorson, M. R.; Zhu, W.; Whipple, D. T.; Kenis, P. J. A.; Masel, R. I. *Science* **2011**, *334*, 643-644.
(23) Zhu, W.; Michalsky, R.; Metin, Ö.; Lv, H.; Guo, S.; Wright, C. J.; Sun, X.; Peterson, A. A.; Sun, S. *J. Am. Chem. Soc.* **2013**, *135*, 16833-16836.

(24) Huan, T. N.; Prakash, P.; Simon, P.; Rousse, G.; Xu, X.; Artero, V.; Gravel, E.; Doris, E.; Fontecave, M. *ChemSusChem* **2016**, *9*, 2317-2320.

(25) Choi, C. H.; Baldizzone, C.; Polymeros, G.; Pizzutilo, E.; Kasian, O.; Schuppert, A. K.; Ranjbar Sahraie, N.; Sougrati, M.-T.; Mayrhofer, K. J. J.; Jaouen, F. *ACS Catal.* **2016**, *6*, 3136-3146.

(26) Rechenbach, D.; Jacobs, H. *J. Alloy. Compd.* **1996**, *235*, 15-22.

(27) It should be noted that the average particle size depends on the total Fe content: small Fe particles of 10-20 nm size covered with a 6-7 nm graphitic layers were observed in $Fe_{1.0}w$ (see ref. 25) while a bimodal size distribution with small (10-20 nm) and large particles (50-100 nm was observed for $Fe_{4.0}d$ (Figure S2a). This bimodal distribution might be related to the presence of two types of crystalline Fe species in Fe4.0d: iron carbide and gamma-Fe (see Figure 2e).

(28) At all potentials the current density is stable during the 5 minutes of the experiment (Figure S3).

(29) Wang, J.; Wang, G. X.; Miao, S.; Li, J. Y.; Bao, X. H. *Faraday Discuss* **2014**, *176*, 135-151.

(30) Tavakkoli, M.; Kallio, T.; Reynaud, O.; Nasibulin, A. G.; Johans, C.; Sainio, J.; Jiang, H.; Kauppinen, E. I.; Laasonen, K. *Angew. Chem. Int. Ed.* **2015**, *54*, 4535-4538.

(31) Wuttig, A.; Yaguchi, M.; Motobayashi, K.; Osawa, M.; Surendranath, Y. *Proceedings of the National Academy of Sciences* **2016**, *113*, E4585-E4593.

(32) Mössbauer spectra of that material was investigated when using that material for O2 reduction (Ref 31). It revealed the presence of a sextet amounting to 17 % of the total absorption area of the spectrum, assigned to magnetic Fe oxide nanoparticles and hence 83% of FeN4 species.

(33) Sahraie, N. R.; Kramm, U. I.; Steinberg, J.; Zhang, Y.; Thomas, A.; Reier, T.; Paraknowitsch, J.-P.; Strasser, P. *Nat. Commun.* **2015**, *6*, 8618.

(34) Costentin, C.; Passard, G.; Robert, M.; Saveant, J. M. *Proc. Nat. Acad. Sci. U.S.A.* **2014**, *111*, 14990-14994.

(35) Dry, M. E. *Catal. Today* **2002**, *71*, 227-241.

Insert Table of Contents artwork here